



Universiteit  
Leiden  
The Netherlands

## Nano-scale electronic structure of strongly correlated electron systems

Tromp, W.O.

### Citation

Tromp, W. O. (2022, December 20). *Nano-scale electronic structure of strongly correlated electron systems*. *Casimir PhD Series*. Retrieved from <https://hdl.handle.net/1887/3503554>

Version: Publisher's Version

License: [Licence agreement concerning inclusion of doctoral thesis in the Institutional Repository of the University of Leiden](#)

Downloaded from: <https://hdl.handle.net/1887/3503554>

**Note:** To cite this publication please use the final published version (if applicable).

---

# 4 Quasi-particle Interference in Overdoped $(\text{Pb,Bi})_2\text{Sr}_2\text{CuO}_{6+\delta}$ : Application of Noise Suppression through Self-Supervised Machine Learning

This chapter contributes to  
Tromp et al. *in preparation*

*The underdoped cuprates are infamous for their complex electronic structure in both real and momentum space, such as a pseudogap, disjointed Fermi arcs and nanometer inhomogeneity amongst others. As the doping increases to the overdoped regime the complexity in momentum space decreases through the disappearance of the pseudogap and the restoration of a full Fermi surface, while the real space electronic structure remains highly complex as discussed in Chapter 3. To try to explain how these two distinct views on the electronic structure fit together, we probe the momentum space structure through quasi-particle interference, thereby staying closer to real space inhomogeneity observed by STS. We implement a state-of-the-art self-supervised machine learning algorithm to suppress the noise present in the QPI images. The noise suppressed images reveal a full Fermi surface with an anti-nodal band shifting rigidly with increased doping. They also reveal a backbending of the band due to the superconducting gap and features around the gap edge associated with an additional density wave. These findings raise new questions on how the different probes of the electronic structure fit together.*

## 4.1 Introduction

Of all electronic phases exhibited by the cuprate family, superconductivity in the overdoped regime was often assumed to be relatively straight-forward<sup>1</sup>, assuming it to be a d-wave BCS superconductor originating from a Fermi liquid normal state, supported by observations of a full Fermi surface<sup>2-4</sup> and quantum oscillations<sup>5</sup> absent in the underdoped regime. Recent results however have shown that the overdoped cuprates are less conventional than this early consensus. In particular, the superconducting state has an anomalously low superfluid density<sup>6-8</sup> and a large uncondensed spectral weight and the normal state shows residuals of strange metal phase at optimal doping<sup>9</sup>. Furthermore, superconductivity is not the only ordered state in the overdoped regime. The  $4a_0$  charge order found in the underdoped regime<sup>10,11</sup> extends into the overdoped, gradually weakening as the doping is increased further<sup>10</sup>. Close to the edge of the superconducting dome a different charge order seemingly appears<sup>10,12</sup>, concomitant with ferromagnetic fluctuation<sup>13,14</sup>. Lastly, the breakdown of superconductivity itself is highly unconventional as we have seen in the previous chapter.

The disappearance of superconductivity in  $\text{Bi}_2\text{Sr}_2\text{CuO}_{6+\delta}$  occurs concomitantly with a Lifshitz transition<sup>3,15</sup>. The flat dispersion associated with this transition has been shown to amplify superconducting fluctuations<sup>4</sup>, and plays a major role in the formation of a granular superconductor<sup>16</sup>. Previous STM results have shown patches of charge order with a wavelength closely associated with the van Hove Singularity (vHS)<sup>12,17,18</sup> accompanying the Lifshitz transition, although it should be pointed out that there is little signature of this in momentum space and RIXS study disagree on the wavevector<sup>10</sup>. The spectral feature of the vHS, a peak in the density of states, has been shown to be highly inhomogeneous, shifting in energy, and disappearing and reappearing over a nanometer length scale (see Chapter 3). This then poses the question how the real space electronic structure, featuring a highly inhomogeneous LDOS, unusual vHS behavior, and nanometer sized puddles of charge order and metallic behavior in the superconducting state, and the momentum space electronic structure, featuring a full single band Fermi surface, no pseudogap, and no Fermi surface reconstruction due to density waves, combine to form one consistent view.

The ideal tool to bridge this gap between real space and momentum space is quasi-particle interference (QPI), being a real space nanoscale measurement used to extract momentum space information. QPI has a long history of valuable insights into the underdoped cuprates, particularly by mapping the gap structure<sup>19,20</sup> and observing the transition from Fermi arcs to a full Fermi surface<sup>2,21</sup>. Furthermore, Fourier transform based analyses of STS data has yielded key results into the charge density and pair density waves<sup>11,22–25</sup> of this doping regime. An advantage of QPI over other momentum space probes is the ability to directly access unoccupied states, even at low temperatures. This is especially useful when characterizing the vHS. ARPES results have shown the Lifshitz transition associated with the vHS<sup>3,15</sup> but cannot map the anti-nodal dispersion near this transition as this requires access to the unoccupied states. Furthermore, for momenta farther away from the anti-node or for doping levels further away from the Lifshitz transition the dispersion ARPES measures is heavily influenced by the gap, and extracting information about the normal state dispersion requires elevated temperatures<sup>26,27</sup>. This too can be circumvented by access to the unoccupied states for which QPI can measure the dispersion for energies high enough that the gap no longer plays a role.

In this chapter we will characterize the anti-nodal dispersion electronic structure of the overdoped cuprates by performing QPI experiments on samples of the single layer cuprate  $(\text{Pb,Bi})_2\text{Sr}_2\text{CuO}_{6+\delta}$  with  $T_c$ 's of 23K, 12K, and 3K (labeled OD23K, OD12K, and OD3K resp.). To do so, we will implement a self-supervised machine learning model to suppress pixel-independent noise present in the QPI images. Our data reveals a full Fermi surface, consistent with previous reports in this doping range<sup>2,15</sup>, and a rigid shifting of the bands with increased doping. Furthermore, we observe a back-bending of the band due to the superconducting gap and shoulder-like features near the gap edge previously associated with a coexisting density wave<sup>27</sup>. We also note the discrepancies between various methods for counting the number of carriers, such as the Luttinger count, the Hall carrier density, or the use of universal doping vs.  $T_c$  relations. Finally, we point out that there is no clear candidate for the ordered state responsible for the features around the gap edge.

## 4.2 Methods

### 4.2.1 QPI Measurements

We perform the STS measurements using an ultra-stable home built cryogenic STM setup<sup>28</sup>. All samples are cleaved at cryogenic temperatures before being loaded in the STM head held at a temperature of 4.2K where all experiments are performed. The samples show an atomically flat surface revealing the Bi-O plane (see **Fig. 4.1a** for an example). The STS measurements were taken over a  $50 \times 50 \text{ nm}^2$  field of view ( $45 \times 45 \text{ nm}^2$  for OD23K) using a fine grid resolving the atomic lattice. The real-space conductance layers (**Fig. 4.1b**) show nm-scale modulations of the LDOS consistent with previous results. All data is drift corrected using the Lawler-Fujita algorithm<sup>24,29,30</sup> (known as geometric phase analysis in other electron microscopy communities). As in Chapter 2, we normalize the conductance layers with their corresponding current layers by taking  $dI/dV(r,eV)/(I(r,eV)/V)$  before taking the FFT to reveal the QPI patterns. **Figs. 4c,d** show the FFT of the  $dI/dV(r,eV)$  and the normalized  $dI/dV(r,eV)/(I(r,eV)/V)$  for the OD12K sample at  $E = 10\text{meV}$  side by side. Note that the signal is sharper in **Fig 4.1d** but loses definition close to the Bragg peaks.

### 4.2.2 Self-supervised Machine Learning for Noise Suppression

The QPI signals shown in **Fig. 4.1** show a considerable amount of noise, making analysis of these images more difficult. The first remedy to limit the amount of noise is to measure longer, take longer or more averages of the spectra that form the initial conductance map. The success of this approach is limited by the maximum measurement time, which is already pushed when taking QPI measurements due to the size of the FOV. An alternative would be to smooth the QPI average by taking a moving average over the image with some window shape (typically a box or Gaussian filter). This however broadens the features in the image, undoing the gain in sharpness by taking the  $dI/dV(r,eV)/(I(r,eV)/V)$ .

To suppress the noise in the QPI images while preserving the sharpness we implement a machine learning algorithm for noise suppression or denoising. The core principle behind machine learning denoising, or image reconstruction in general, is that the structure of an image can be described with a number of parameters that is much less than the number of pixels of the image. As such, it should be possible to learn the underlying structure and reconstruct a noise free (or at least a noise suppressed) version of the image.

A neural network can be seen as a function  $f$  with an input  $x_i$  and output  $y_i$  governed by a set of parameters  $\theta$ . The quality of the output  $y_i$  is given by the error or loss  $E$  calculated by comparing to the desired output or label  $\hat{y}_i$  through the loss function  $L$ :

$$E = \mathcal{L}(\hat{y}_i, y_i) = \mathcal{L}(\hat{y}_i, f(x_i|\theta)) \quad (4.1)$$

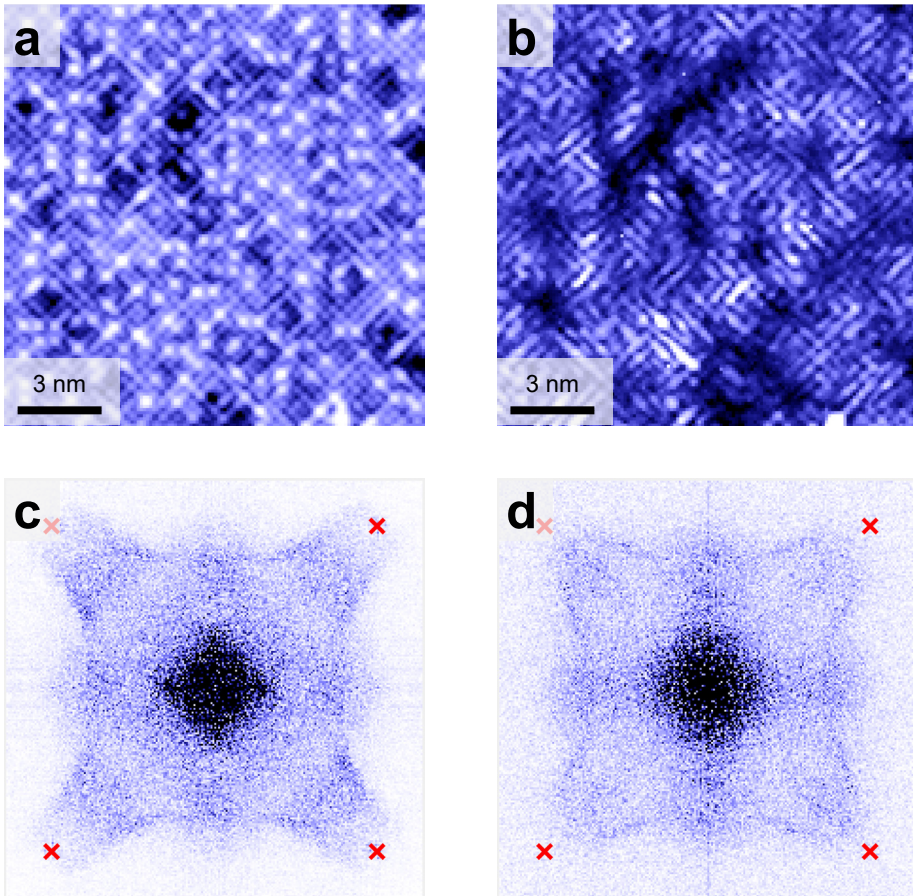


**Figure 4.1 Bi2201 Topography and LDOS.**

*a)* High resolution topography of a 15x15 nm field of view of the OD12K sample. The atomic lattice of the Bi-O plane is clearly resolved with the Pb dopants visible as bright white dots. *b)* LDOS modulations at  $E = 10$  meV in the same FOV as *a)*. *c,d)* QPI signal of a 45x45 nm FOV of the OD12K sample at  $E = 10$  meV revealed by taking the FFT of the  $dI/dV$  layer and the  $(dI/dV)/(I/V)$  layer respectively after drift correction. The red crosses indicate the Bragg peaks from the atomic lattice.

The best output  $y_i$  is then the output that minimizes the error  $E$ . Typically this is not the case of the output  $y_i$  given by the initial set of parameters  $\theta$ . To minimize  $E$ , during each cycle or epoch the loss is calculated and the parameters  $\theta$  adjusted to yield a lower loss in the next epoch through gradient descent. When the error has been minimized the network has been trained. When the dataset consists of multiple elements, such as multiple QPI images, the dataset is often split into batches. During an epoch each image within a batch is fed to the network and a loss over the batch is calculated, after which the parameters  $\theta$  are updated and the next batch is used. Over the course of one epoch each element of the dataset has been fed to the network. It is common practice to split off a part of the dataset into a validation dataset. The loss of the network over the validation network is calculated at regular intervals during training, but is not used to update the network parameters. As such, the loss over the validation dataset, or validation loss, represents the performance of the network on data not used for training, and is closely monitored during the training process.

The most common approach is to use supervised learning<sup>31-33</sup>, i.e. using pairs of corrupted and clean images as inputs and labels (**Fig. 4.1a**). The network is trained by minimizing the loss between the clean example and the output when a noisy image is inputted. When a corrupted image without a clean example is then fed to the network, the output will be a noise-free version of the input provided the underlying structure of the input is similar enough to that of the images used to train the network. Recent work has shown that the clean images don't have to be clean at all<sup>34</sup>. Having multiple noisy version of the same image can be enough to learn the structure of the image. If one characterizes the noise well enough to generate artificial noise similar enough to the noise in the original image, one can use this to generate the necessary training data to train the network and denoise the original data.

The issue with this approach is that it requires training data that is often not available in a scientific setting. Clean versions of the images are most often not available as scientific measurement setups are often already operating at their limits. Even acquiring multiple noisy copies of the same image is often not possible due to time constraints or changing experimental conditions. To work with STM data we need a self-supervised approach, i.e. one that doesn't require training data. Instead, we will assume some structure of the noise to denoise the QPI images. The method we implement here, called Noise2Void or Noise2Self<sup>36,37</sup>, assumes that the noise is pixel independent, meaning that

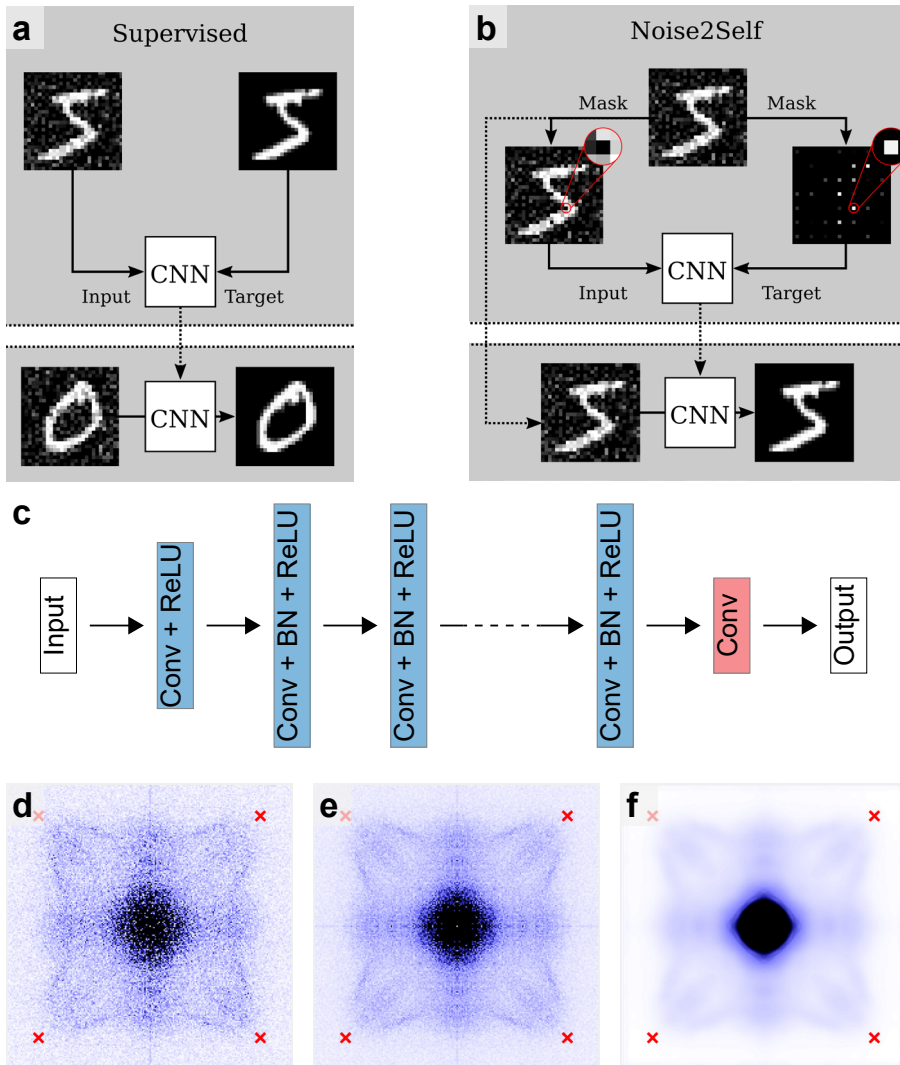


**Figure 4.2** Self-supervised denoised QPI images.

**a)** Schematic of the traditional, supervised approach noise suppression. The network is trained on a pair of noisy inputs and clean targets. A different noisy image not part of the training data can then be denoised using the network. **b)** Schematic of Noise2Self. The input and targets now consist of a noisy image with some pixels masked and those masked pixel. The trained network can now be used to denoise the original image. **a, b** adapted from Ref. 35. **c)** DnCNN architecture used consisting of 17 layers containing each a convolutional (Conv) layer with 64 features, batch normalization (BN, except the first layer), and a ReLU activation function. These are followed by a convolutional layer generating the output. **d)** Example of QPI data before denoising (OD12K sample,  $E = 10$  meV, same as Fig. 4.1d). **e)** Symmetrized version of **d)** for comparison to **f)**. **f)** Denoised and symmetrized using **d)** as input. The noise is clearly suppressed with the image slightly blurred.

the strength of the noise on one pixel will not tell anything about the strength of the noise on other pixels, neighbors included. For the mathematical reasoning behind this approach and details of the implementation we refer to the original papers<sup>36,37</sup>. The idea of Noise2Self (**Fig. 4.2b**) is to alter the value of some pixels during each training step (usually setting the pixel to zero or to the average of its neighbors). The network will then assign new values to those pixels and the training loss is evaluated at those pixels. Which pixels are altered varies during training. The network will fill in the blanks of the missing pixels using the underlying structure it learned, without any pixel independent structure as it doesn't have access to the pixel it is trying to fill in. As such, the network can reconstruct a clean version of the noisy image. This approach to noise suppression has already found successful application in tomography<sup>35,38</sup> and can also be used to optimize parameters for certain filters or dimension reduction techniques<sup>37</sup>.

It is important that this approach only works for pixel independent noise. Anything else will be interpreted as part of the structure of the image. If there is structured noise present in the image, for example some repeating pattern, Noise2Self will preserve this structure, while approaches based on clean training data can also suppress this type of noise<sup>36</sup>. Most notably this also holds for any artifact that might be introduced into the data during the measurement.

The network architecture we will use is a DnCNN network<sup>32</sup> (see **Fig. 4.2c**), similar to the one used in the original Noise2Self paper<sup>37</sup>, implemented using Python's TensorFlow package. We will use 17 layers, with 64 features each. The loss is calculated using the mean squared error, and we will use a learning rate of 0.01 during training. The data is layer-wise mean subtracted before taking the FFT and afterwards normalized to [0,1] layer-wise. The QPI data is split into batches of 10 images which are shuffled each training step. The network is trained for 100 epochs. The noise suppressed images are then symmetrized. An example of the data used as output and fully processed data is shown in **Figs. 4.2d-f**. The algorithm has worked as intended, with the noise in **Fig. 4.2f** suppressed compared to **Fig. 4.2d,e**. The reconstruction is not perfect, as the image is slightly blurred compared to the inputs.

## 4.3 Results

### 4.3.1 Fermi surface

We start by looking at the QPI signal at  $E = 0\text{meV}$ , showing the interference from states on the Fermi surface. In this doping range we expect a full Fermi surface<sup>2,21</sup>, meaning the QPI signal will trace the shape of the Fermi surface with  $q = 2k_F$ . The  $E = 0\text{meV}$  layers shown in **Fig. 4.3a-c** for the OD3K, OD12K, and the OD23K samples indeed have a signal at  $q = 2k_F$  consistent with a full Fermi surface of a single band. In particular there is no sign of octet model scattering vectors characteristic of the pseudogap in the underdoped regime. The horizontal and vertical line through the center in **Fig. 4.3b** are the result of an unknown artifact only present in the OD12K measurement. Note that the signal at the anti-node next to the Bragg peaks are very faint or absent. This seems to be the result of two factors: first, these scattering vectors are already weaker in the  $dI/dV$  QPI signals (see **Fig. 4.1c**) and second, these vectors become even weaker after normalizing to  $(dI/dV)/(I/V)$ . The reason behind these two factors are unclear. Fainter signal at the anti-nodes can be the result of a combination of details of the scattering process and conditions of the STM tip. Why normalization weakens the signal at large  $q$  vectors is also not clear, though it should be noted that something similar happens in the rhodates in Chapter 2, as seen in **Fig. 2A.1**.

We trace the Fermi surfaces by fitting the peak position of the  $q = 2k_F$  signal along the cuts indicated by the red lines in **Fig. 4.3c**. The result is shown in **Fig. 4.3d**, where we have divided the values for the  $q$  vectors by 2 and rotated them to show the band from which the scattering originates in the 1<sup>st</sup> Brillouin Zone (BZ). We also show a tight binding fit<sup>2,27</sup> to the Fermi surfaces. There is very little difference between the 3 Fermi surfaces and their fits, especially for the OD3K and OD12K samples. This is due to the fact that the band only moves very little for these doping values, especially in the nodal region, combined with the uncertainty of the fit when extracting the Fermi surface.

To see the shift of the band as a function of doping we plot the  $\varepsilon_0$  parameter of the tight binding model, which governs the band shift, as a function of doping in **Fig. 4.4a**, together with the  $\varepsilon_0$  parameters determined by He et al.<sup>2</sup> with the QPI patterns of the same  $(\text{Pb,Bi})_2\text{Sr}_2\text{CuO}_{6+\delta}$  compound using the same tight binding model. The doping levels on the x-axis are determined using the  $T_c$  of the samples and the Presland formula for the relation between doping and

$T_c$ <sup>39</sup>. We find lower values for  $\varepsilon_0$  and a different slope as a function of doping. We could fit a straight line through our point to quantify the difference in offset and slope. Given the number of data points however this would not be very reliable. Regardless, our results are not fully consistent with their previous results, where we point out, in addition to the earlier mentioned precision of our Fermi surface extraction, the values for  $\varepsilon_0$  determined by He et al. are obtained by ‘fitting’ the tight binding model to their data by eye.

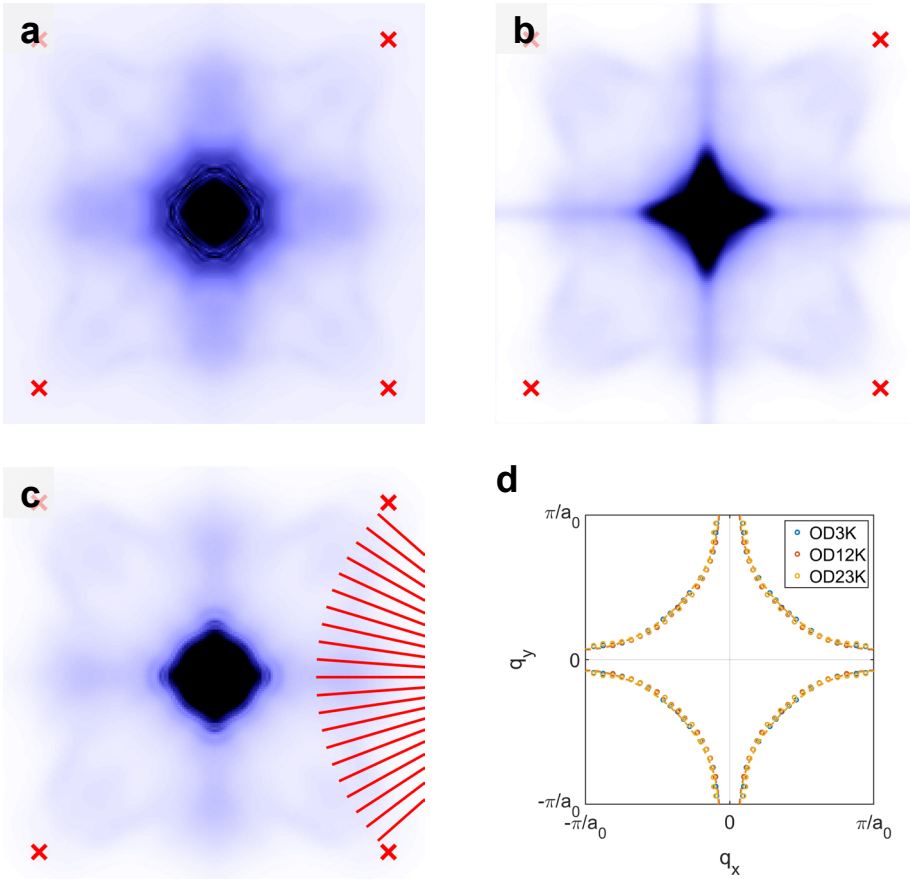


**Figure 4.3 Bi2201 QPI Fermi surfaces.**

**a-c)** The QPI signal at  $E = 0\text{meV}$  for the OD3K, OD12K, and OD23K samples respectively after normalizing to  $(dI/dV)/(I/V)$  and denoising using the Noise2Self algorithm. The red crosses indicate the position of the Bragg peaks. The red lines in **c)** show the cuts used to extract the Fermi surface scattering vectors. **d)** The Fermi surfaces determined using the QPI pattern in **a-c)** by dividing the scattering vectors by two, rotating them and duplicating them to show two parts of the Fermi surface. The dashed lines show the tight binding fits to the Fermi surface for each sample.

A different way to show the shifting of the band is to look at the area of the Fermi surface and calculate the Luttinger count. The result is shown in **Fig. 4.4b**, together with the Luttinger counts determined by He et al. Similarly to the result for  $\varepsilon_0$  we find a discrepancy between our result and theirs, not surprisingly given that  $\varepsilon_0$  and Luttinger count are related. It is important to note that for  $(\text{Pb,Bi})_2\text{Sr}_2\text{CuO}_{6+\delta}$  the Luttinger count does not match the doping levels from the Presland formula<sup>39</sup>, as was noticed previously for both single layer and double layer Bi-based cuprates  $(\text{Pb,Bi})_2\text{Sr}_2\text{CuO}_{6+\delta}$  and  $\text{Bi}_2\text{Sr}_2\text{CaCu}_2\text{O}_{8+\delta}$ <sup>2,3</sup>. Still this universal formula for doping vs.  $T_c$  is useful as long as the relation depicted in **Fig. 4.4b** shows a straight line.

### 4.3.2 Anti-nodal Dispersion

Next we look at the anti-nodal dispersion by taking a series of cuts perpendicular to the  $(0,0)-(2\pi,2\pi)$  line shown in **Fig. 4.5a**. The cuts are taken more towards the midway point between nodal and anti-nodal since the signal fades away moving closer to the anti-node. The cuts, examples of which are shown in **Fig. 4.5b-d**, feature both a gap around Fermi level and a band crossing  $E_F$ . The cuts in **Fig. 4.5b,c** have a strongly reduced intensity directly around  $E_F$  due to the gap but note that there are still clear QPI for the  $E = 0\text{meV}$  layer, as seen in **Fig. 4.3a,b**. The cut in **Fig. 4.5d** also has reduced intensity near  $E_F$  but not

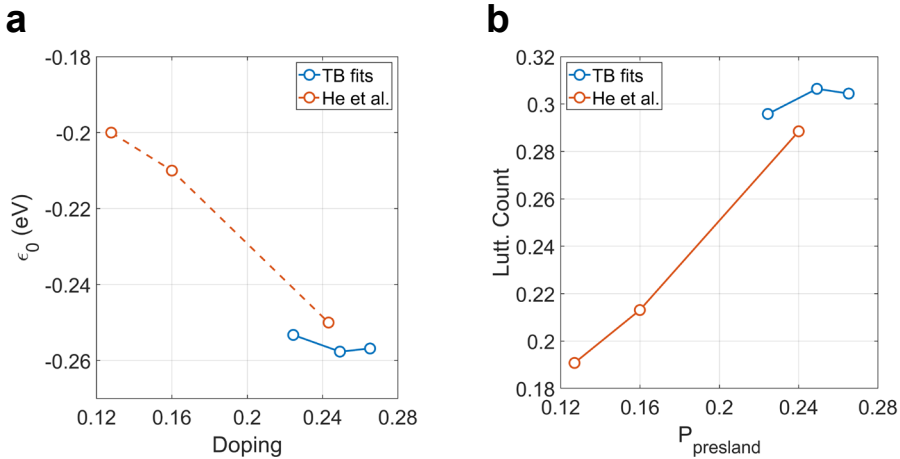


**Figure 4.4** Tight binding  $\varepsilon_0$  and Luttinger count.

**a)** The  $\varepsilon_0$  parameter of the tight binding fits shown in **Fig. 4.3d** as a function of doping in blue. The doping values on the x-axis are calculated using the  $T_c$  of the samples and the Presland formula<sup>39</sup>. The  $\varepsilon_0$  values determined previously<sup>2</sup> for the same compound are shown in red. **b)** The Luttinger count calculated using the area of the Fermi surface as a function of doping in blue. Previously determined values are shown in red.

at  $E_F$ . This is most likely an artifact from the noise suppression, a point we will get back to in section 4.4. The fact that there is still QPI associated with a full Fermi surface at  $E = 0\text{meV}$  for superconducting samples is a result of the pronounced gap filling occurring in this doping range described in Chapter 3.

Next, we fit the peak position of momentum distribution curves (MDCs) of the cuts to extract the band crossing  $E_{F'}$  shown in **Fig. 4.5b-d** as the blue dots and plotted together in **Fig. 4.6a** for the cut highlighted in **Fig. 4.5a**. For cuts

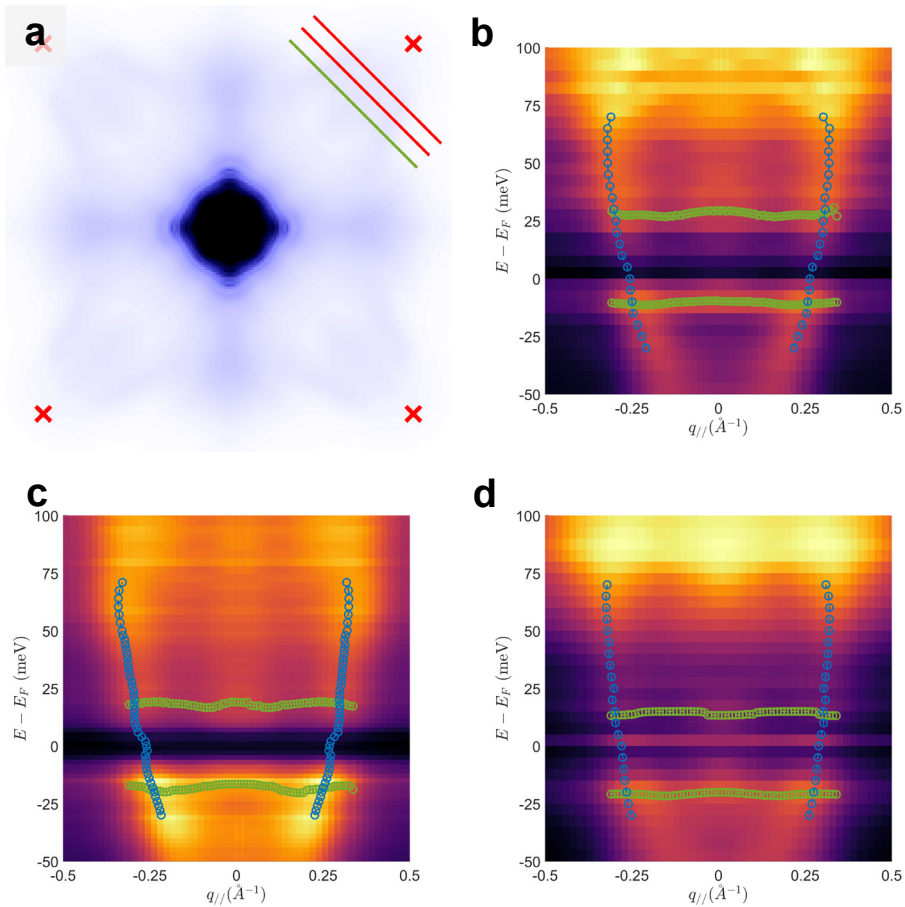


**Figure 4.5** Anti-nodal dispersion.

**a)** The  $E = 0\text{ meV}$  QPI layer for the OD23K sample indicating the lines along which the cuts are taken used to extract the bandstructure. The green line shows the cut shown in **b-d**). The red crosses indicate the position of the Bragg peaks. **b-d)** The cuts along the green line in **a)** for the OD3K, OD12K, and OD23K sample respectively. The blue points show the peak position of the fitted MDCs, the green points show the peak position of the fitted EDCs.

taken at the anti-node where the bandstructure has a saddle point (the vHS) the dispersion is parabolic, disregarding any possible back bending due to a gap. The cuts in **Fig. 4.5** however are taken away from the anti-node so that

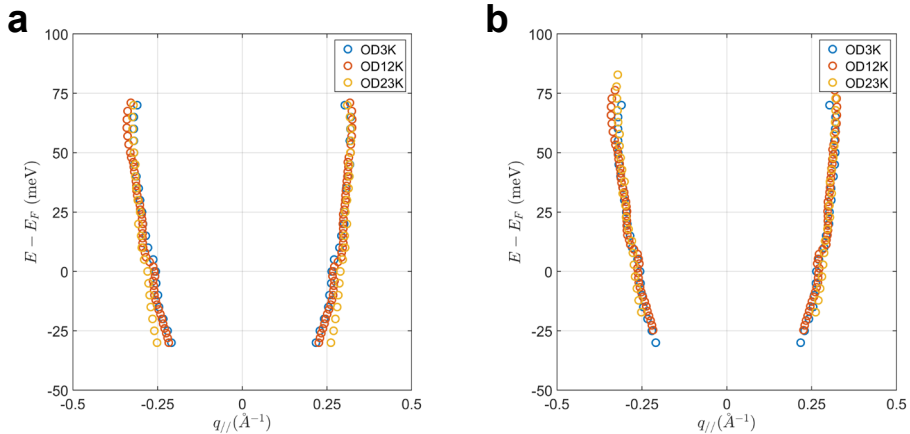


**Figure 4.6 Bandshift measurement.**

*a)* The anti-nodal dispersion for the OD3K, OD12K, and OD23K extracted from the cuts shown in **Fig. 4.5b-d** by fitting the MDC peak positions. The bandshifts are measured by finding the shift to the OD12K and OD23K dispersions that minimizes the sum of the point-wise distances to the OD3K dispersion. The result of the shifting procedure for the data shown in **a)** is shown in **b)**.

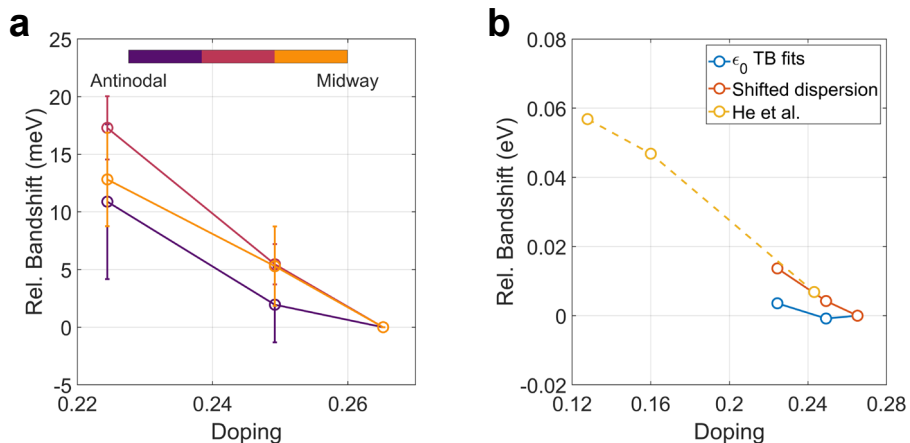


**Figure 4.7 Bandshift doping dependence.**

*a)* The extracted QPI bandshifts relative to the OD3K sample for the three cuts indicated in **Fig. 4.5a**, with the cut labeled anti-nodal being closest to the Bragg peaks and the one labeled midway furthest. *b)* The average of the shifts shown in **a)** compared to the shifts determined by tight-binding fits to the QPI Fermi surface, and compared to the shifts determined by Ref. 2.

the dispersion is no longer guaranteed to be parabolic. Therefore we take an agnostic approach to measuring the bandshift. We add a shift manually to the dispersion of the OD12K and OD23K and calculate the relative distance for points at constant  $q_{\parallel}$ . The true bandshift is then the shift which minimizes the sum of the squared distances. The shifted dispersion for the highlighted cut in **Fig. 4.5a** are shown in **Fig. 4.6b**. We then repeat this procedure for all cuts taken. The resulting bandshifts relative to the OD3K sample are shown in **Fig. 4.7a** for each cut, where the errorbars give the 95% confidence interval for the calculated shifts. We find that, within error, the shifts follow a straight line, where the caution of the number of data points again holds. The straight line of the shifts, or the rigidity of the bandshifts, becomes more apparent when we average the calculated values over the different cuts used and plot them against previous results<sup>2</sup>, as we have done in **Fig. 4.7b**. We find a good agreement with the slope of the  $\varepsilon_0(p)$  line determined by He et al. Note that the data points for  $\varepsilon_0$  were shifted so that all the curves coincide at a shift of 0 for the OD3K sample. This is done as the shift measured from movement of the bandstructure only gives relative values of this shift, versus more absolute values when calculating  $\varepsilon_0$  from tight-binding model.

Another feature of the anti-nodal electronic structure becomes apparent when we look at the peak positions of the energy distribution curves (EDCs, green points in **Fig. 4.5b-d**). We find shoulder features at lower  $q$  near both gap edges for all samples. The shoulder above the Fermi level can be attributed to back bending of the band due to the band, although it should be noted that this occurs at unusually large energies for the OD3K sample. The exact shape of the backbended band reveals important information on the nature of the gap. For a purely superconducting gap we expect a particle-hole symmetric bending of the band, while for other ordered states the bending does not necessarily have this symmetry. The data presented here however lacks the resolution to conclusively determine whether the bending is particle-hole symmetric.

Another clue to the nature of the gap stems from the feature near the gap edge below the Fermi level. Here, for a superconducting gap, we expect band bending only to occur for momenta larger than  $k_F$  (or  $q_F$  in our case). We find that this shoulder is present in all cuts for each sample. The large extension in  $q$  and its lack of dispersion means it is unlikely to stem from purely bandstructure QPI. Such a feature has been observed before by ARPES in the same compound<sup>27</sup>, where it was attributed to superconductivity co-

existing with an additional density wave. The precise nature of the density wave determines some of the details of the back bending, but all scenarios share this additional low momentum feature. There are indications of an additional ordered state next to superconductivity in this doping range for Bi2201, however their link to this feature remains to be investigated

## 4.4 Discussion

### 4.4.1 Artifacts of Noise Suppression

The observation that the shoulder feature above  $E_F$  occurs at an unusually large energy for the OD3K sample warrants a closer examination of the denoising algorithm. Another unusual aspect of the OD3K data is that the gap seems to be asymmetric. The suppression of intensity due to the gap seems to extend to larger energies above  $E_F$  than below. A comparison of the anti-nodal cuts from noise suppressed data with the  $(dI/dV)/(I/V)$  data used as input, shown in **Fig. 4.8**, shows that the asymmetry is a result of the noise suppression. The comparison shows that the dispersion is well-preserved by the noise suppression, together with the shoulder features around the gap, although the one above  $E_F$  has moved up in energy. The comparison also shows that the relative intensities of the energy layers is changed quite drastically, a point

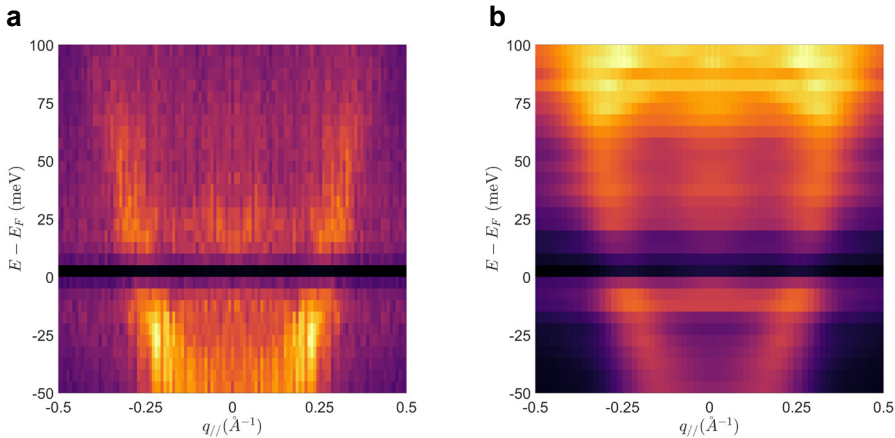


**Figure 4.8** Before and after comparison anti-nodal cuts.

**a)** Anti-nodal cut taken from the OD3K  $(dI/dV)/(I/V)$  data before noise suppression along the green line indicated in **Fig 4.5a**. **b)** The same cut after noise suppression of the full data set. The main features are preserved (dispersion, shoulders at the gap edge), but the relative intensities of the energy layers has changed drastically.

emphasized when we plot the average value of the energy layers, shown in **Fig. 4.9a**. It is clear that relative layer intensities are not preserved during the noise suppression. This is a result of the 2D network design used combined with an imperfect reconstruction of the images. Ultimately, the images are fed one by one to the network and shuffled between epochs. Any information about the relative information of the image in the 3D dataset, or any information about neighboring layers is lost during the denoising. As a result, the intensity of a layer relative to the other layers is can exhibit sharp jumps or vary more freely than pixel intensities within a layer, for which neighborhood information is provided to the network to suppress sharp jumps. The fact that there is still some gap structure present in the noise suppressed data is in part due to the normalization applied before the data is fed to the network. The data is layer-wise normalized to the interval  $[0, 1]$ , which is then applied in reverse to the network output. The application of the reverse normalization restores some of the relative intensity, but not all.

The remedy for this would be to implement a 3D network, which takes the dataset as a whole as input. Training such a network would require unreasonably long computation times for anything but a very small dataset, or require running on a supercomputer. A good intermediate solution is a 2.5D network, as was done for the Noise2Self tomography implementation<sup>38</sup>. In such a network, the input is comprised of three images: the image to be denoised and its neighbors in the 3D dataset. The addition of the neighboring layers to the actual input does two things: first it improves the overall quality of the denoising as more information is known to the network through the addition of extra neighbors to the masked pixels. Second it can add context to the input in the third dimension not present for a strictly 2D network. As such, a 2.5D network can suppress sharp changes in intensity along the third direction.

Further improvements to the network are possible. While common for image reconstruction tasks, the DnCNN architecture used here is but one of many. Other common architectures include Red30<sup>40</sup> and U-Net<sup>41</sup>. As for the layers used within DnCNN there is room to optimize the number of layers used, the number of feature per layer, or the use of dropout. Other optimizations include the activation function or the loss function. The mean squared error used here is a default choice for image reconstruction, but given the size of the images, switching to loss functions which tries to capture structural similarity might be worthwhile.

In the current implementation of the noise suppression the network is trained on each dataset separately. A possible route towards improved performance and more general applicability is to pool the data together and train the network once on the new bigger dataset. The rationale being that, the samples being from the same compound family, the QPI images across the samples share enough of a common underlying structure. For the current data this would require down sampling some images to ensure equal image size throughout the whole dataset. This approach would open the door to a more generally applicable network for QPI images from distinct compounds having distinct bandstructures through transfer learning. Transfer learning extends the range of applicability by training a deep network on a large dataset (e.g. a collection of QPI dataset from different samples and/or compound families). This network can then be applied to a dataset not seen before, and not necessarily having a structure present in the training dataset, by retraining only the top layer(s) of the network. The deep parts of the network then encode the general common elements of QPI images (e.g. common noise sources) while the top layers take care of dataset specific structures. This would also have the added benefit of speeding up the computation time for each new dataset once the deep network has been trained.

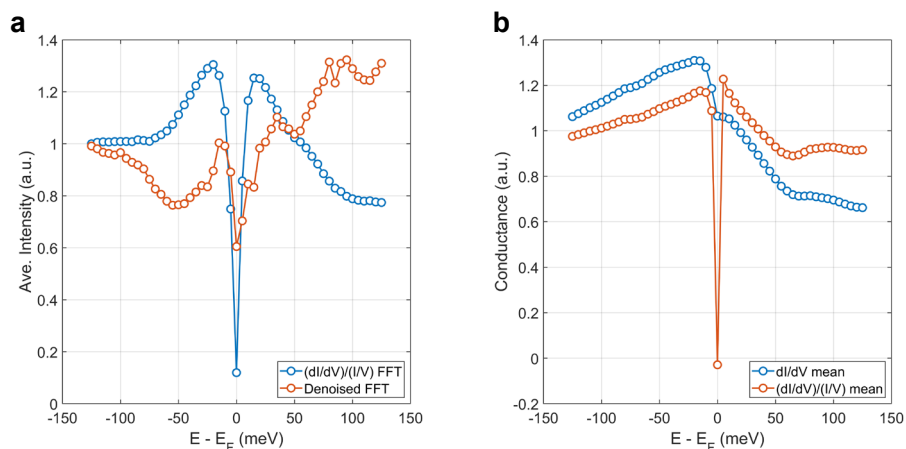


**Figure 4.9** Layer intensities before and after noise suppression.

**a)** The average intensity of the QPI layers of the OD3K sample before and after noise suppression as a function of energy. While the averages for the  $(dI/dV)/(I/V)$  before denoising resembles the real space average, the averages after denoising have lost that resemblance. **b)** Comparison of the real space averages for the  $dI/dV$  data and the  $(dI/dV)/(I/V)$  data for the OD3K sample. Normalizing layer-wise by the current has made the gap much more pronounced.

As a side note, the uncharacteristically deep gap for the OD3K sample shown by the blue curve in **Fig. 4.9a** is a result of the normalization of the  $dI/dV$  spectra with the current layers  $I$ , as shown by the comparison of the real space averages of the  $dI/dV$  spectra and the  $(dI/dV)/(I/V)$  spectra shown in **Fig. 4.9b**. The current  $I$  and the bias voltage  $V$  are in principle roughly linearly related in the small energy window around  $V = 0$ , so that the ratio  $I/V$  remains constant even as  $V$  and with it  $I$  approach zero. Even so, small fluctuations in the value for  $I$  registered by the STM hardware can lead to large differences in the normalized  $(dI/dV)/(I/V)$ . To temper these differences we add a  $10\mu\text{V}$  offset to the bias during normalization, to only partial success as seen by the sharpness of the gap in the  $(dI/dV)/(I/V)$  average depicted in **Fig. 4.9b**.

#### 4.4.2 Carrier Concentration and Bandshifts

Bandshifts in overdoped cuprates have been reported before in both  $\text{Bi}_2\text{Sr}_2\text{CuO}_{6+\delta}$ <sup>2,42</sup> and  $\text{La}_{2-x}\text{Sr}_x\text{CuO}_4$ <sup>42,43</sup>, although their doping dependence is not trivial. The magnitude of the shifts increase strongly past overdoping at  $p=0.16$ , for  $\text{La}_{2-x}\text{Sr}_x\text{CuO}_4$  even becoming non-zero only then<sup>42</sup>. Interestingly, this occurs before the closing of the pseudogap around  $p^* = 0.19 - 0.20$ <sup>44</sup>, suggesting the bandshifts are decoupled from the restoration of the full Fermi surface. Instead, the increased magnitude of the bandshifts seems to coincide with the start of a gradual change in the Hall carrier density from  $n_{\text{H}} = p$  to  $n_{\text{H}} = 1+p$ <sup>45</sup>. The rigidity of the shift, behavior typical of a Fermi liquid combined with the gradual change of  $n_{\text{H}}$  to  $n_{\text{H}} = 1+p$  and the emergence of a  $T^2$  component of the resistivity<sup>45</sup> suggests that these doped carriers constitute a coherent Fermi liquid-like normal state, coexisting with an incoherent electron fluid with  $T$ -linear resistivity,  $n_{\text{H}} = p$ , and little to no shifts in the chemical potential<sup>42,45</sup>. This tentative relation between bandshift magnitude and  $n_{\text{H}}$  would imply another change in shift magnitude at the end of the superconducting dome, where  $n_{\text{H}}$  saturates to  $n_{\text{H}} = 1+p$ . QPI investigation beyond the superconducting dome will test this relation in the metallic state past the Lifshitz transition.

Future STM work can relate these two fluids to spectral features (superconducting or pseudogap, vHS) by identifying the real space distribution of these features and applying masks to the  $dI/dV$  data before taking the FFT to reveal the QPI patterns, a technique used previously to study charge order in  $\text{Bi}_2\text{Sr}_2\text{CuO}_{6+\delta}$ <sup>11,23</sup>. The machine learning techniques detailed in this chapter can help overcome the challenges of the additional noise introduced by such real space masking.

Interestingly, there is a mismatch between the Luttinger count extracted from STM and ARPES and universal formulas for doping vs  $T_c$ , as was noted before<sup>2,42,44</sup>. Adding to the puzzle, the relation between Luttinger count and universal doping formulas does appear to be linear across the full superconducting dome<sup>2</sup>, implying that the amount of holes doped per dopant is constant over this part of the phase diagram. This appears at odds with the doping dependence of the bandshifts and Hall carrier concentration, which feature a sharp change at optimal doping<sup>42,45</sup>. The former discrepancy is especially concerning as both the Luttinger count and the bandshifts are typically determined by a tight-binding characterization of the Fermi surface, although we have shown that the bandshift still holds without the use of tight-binding models. A possible solution to this is by noting that the tight-binding hopping parameters can be doping dependent, for which there is precedent<sup>42,43</sup>. This doping dependence seems to smooth however, rather than featuring a pronounced change at  $p = 0.16$  the bandshift and  $n_H$  have. Why the drastic increase in free carrier deduced from  $n_H$  is not reflected in a similarly rapid change in the Fermi surface area remains an open question. One proposal that the Luttinger count only counts coherent carriers<sup>44</sup> seems unlikely as the relation between Luttinger count and universal formulas is linear over a doping range larger than the one in which coherent carriers are added. Investigation into the non-superconducting overdoped regime will reveal how these relations hold when there are no incoherent carriers present. Alternatively, the high Luttinger count is the result of surface effects, to which both STM and ARPES are susceptible, versus bulk measurement on which  $n_H$  and the universal doping formulas are based. These surface effects would then most likely be caused or enhanced by the physics of the cuprates, as we have shown in Chapter 2 that bulk and surface probes of the bandstructure are in agreement with each other for Fermi liquid systems.

#### 4.4.3 Density Waves in Overdoped $\text{Bi}_2\text{Sr}_2\text{CuO}_{6+\delta}$

The observation of the shoulder features at the gap edge (**Fig. 4.5b-d**) has been attributed to the presence of some density wave in addition to the backbending of the band due to superconductivity. This raises the question what that density wave is. There are two main candidates in overdoped single layer cuprates: a charge density wave (CDW) or ferromagnetic fluctuations (FMF). CDW order has been observed across the overdoped regime in both  $\text{Bi}_2\text{Sr}_2\text{CuO}_{6+\delta}$ <sup>10-12</sup> and  $\text{La}_{2-x}\text{SrCuO}_4$ <sup>46</sup>, albeit with markedly different doping dependence. In the latter compound X-ray diffraction

studies have found CDW order extending over the entirety of the overdoped superconductivity regime with a nontrivial doping dependence, but only disappearing concomitantly with superconductivity at the edge of the dome. In contrast, in  $\text{Bi}_2\text{Sr}_2\text{CuO}_{6+\delta}$  the overdoped CDW shows re-entrant behavior, being disconnected from the underdoped CDW that gradually disappears in the overdoped<sup>11</sup>. The re-entrant behavior only starts to show around a  $T_c$  of 15K<sup>10,12</sup>. The fact that we observe the shoulder feature for the OD23K sample disqualifies the strongly overdoped CDW as the cause for all three samples. It could be possible that the feature in the OD23K sample is caused by remnants of the overdoped CDW, while for the higher doped samples it is caused by the re-entrant CDW. More detailed calculations investigating the difference in band bending between these two CDWs combined with QPI or ARPES measurements with high enough resolution to resolve those differences are needed to resolve this issue. The shoulder-like feature above  $E_F$  accessible by QPI or high-temperature ARPES (if the appropriate temperature range exists) can provide additional information on the exact structure of the backbending. It should be noted that X-ray diffraction and STM disagree on the wavevector of re-entrant CDW<sup>10,12</sup>. Particularly, the STM observation can be interpreted as QPI resulting from anti-nodal scattering, given that a clear momentum space signature of this CDW is absent in the STM measurements<sup>12</sup>. Also note that there is a gap in the doping range in the available X-ray data, leaving room for an interpretation where the proposed CDW is not re-entrant, but a continuation of the underdoped CDW. As the observation of the shoulder-like feature only provides indirect evidence for a CDW, the question whether a CDW exists across the overdoped regime in  $\text{Bi}_2\text{Sr}_2\text{CuO}_{6+\delta}$  remains open.

An alternative explanation involves the FMF found in overdoped  $\text{La}_{2-x}\text{SrCuO}_4$ <sup>13,14</sup> and  $\text{Bi}_2\text{Sr}_2\text{CuO}_{6+\delta}$ <sup>47</sup>. In the latter case the FMF appear to extend over a doping range compatible with the samples studied here. The FMF have not however been shown to form static order at higher doping or lower temperatures. How fluctuating order impacts the backbending remains to be investigated.

## 4.5 Conclusion & Outlook

In conclusion, we have investigated the anti-nodal electronic structure of overdoped  $\text{Bi}_2\text{Sr}_2\text{CuO}_{6+\delta}$  using QPI. We have implemented a state-of-the-art self-supervised machine learning algorithm to suppress the noise in the QPI

images. Using the noise suppressed data we have shown that the anti-nodal band shows a rigid bandshift with overdoping. Additional studies into the non-superconducting regime are needed to resolve discrepancies between the doping dependences of the bandshifts<sup>42,43</sup>, the Luttinger count<sup>2,44</sup>, and the Hall carrier density<sup>45</sup>. The backbending of the band due to the superconducting gap features shoulder-like features near the gap edge associated with the presence of a density wave<sup>27</sup>, whose nature remains unknown. More detailed calculations, focused particularly on the types of CDW with a doping dependent scattering vector and weak coherence proposed by X-ray and STM experiments combined with higher resolution experiments are needed to reveal the origins of the band bending and the associated density wave. The findings presented here reveal a picture where QPI and ARPES appear in agreement over the momentum space electronic structure, but in disagreement with other probes such as transport and X-ray diffraction over the carrier density and the presence and doping dependence of an additional ordered state next to superconductivity. More detailed studies of the electronic structure around the gap from both experimental and theoretical/computational viewpoint over an extended doping range are needed to bridge the gap between the various probes.

## 4.6 References

- [1] Keimer, B., Kivelson, S. A., Norman, M. R., Uchida, S. & Zaanen, J. From quantum matter to high-temperature superconductivity in copper oxides. *Nature* **518**, 179–186 (2015).
- [2] He, Y. *et al.* Fermi surface and pseudogap evolution in a cuprate superconductor. *Science* **344**, 608–611 (2014).
- [3] Drozdov, I. K. *et al.* Phase diagram of  $\text{Bi}_2\text{Sr}_2\text{CaCu}_2\text{O}_{8+\delta}$  revisited. *Nat. Commun.* **9**:5210 (2018).
- [4] He, Y. *et al.* Superconducting Fluctuations in Overdoped  $\text{Bi}_2\text{Sr}_2\text{CaCu}_2\text{O}_{8+\delta}$ . *Phys. Rev. X* **11**, 031068 (2021).
- [5] Vignolle, B. *et al.* Quantum oscillations in an overdoped high- $T_c$  superconductor. *Nature* **455**, 952–955 (2008).
- [6] Uemura, Y. J. *et al.* Magnetic-field penetration depth in  $\text{TI}_2\text{Ba}_2\text{CuO}_{6+\delta}$  in the overdoped regime. *Nature* **364**, 605–607 (1993).
- [7] Lemberger, T. R., Hetel, I., Tsukada, A., Naito, M. & Randeria, M. Superconductor-to-metal quantum phase transition in overdoped  $\text{La}_{2-x}\text{Sr}_x\text{CuO}_4$ . *Phys. Rev. B* **83**, 140507 (2011).

- [8] Bozovic, I., He, X., Wu, J. & Bollinger, A. T. Dependence of the critical temperature in overdoped copper oxides on superfluid density. *Nature* **536**, 309–311 (2016).
- [9] Mahmood, F., He, X., Božović, I. & Armitage, N. P. Locating the Missing Superconducting Electrons in the Overdoped Cuprates  $\text{La}_{2-x}\text{Sr}_x\text{CuO}_4$ . *Phys. Rev. Lett.* **122**, 027003 (2019).
- [10] Peng, Y. Y. *et al.* Re-entrant charge order in overdoped  $(\text{Bi,Pb})_{2.12}\text{Sr}_{1.88}\text{CuO}_{6+\delta}$  outside the pseudogap regime. *Nat. Mater.* **17**, 697–702 (2018).
- [11] Webb, T. A. *et al.* Density wave probes cuprate quantum phase transition. *Phys. Rev. X* **9**, 021021 (2019).
- [12] Li, X. *et al.* Evolution of Charge and Pair Density Modulations in Overdoped  $\text{Bi}_2\text{Sr}_2\text{CuO}_{6+\delta}$ . *Phys. Rev. X* **11**, 11007 (2021).
- [13] Kopp, A., Ghosal, A. & Chakravarty, S. Competing ferromagnetism in high-temperature copper oxide superconductors. *Proc. Natl. Acad. Sci.* **104**, 6123–6127 (2007).
- [14] Sonier, J. E. *et al.* Direct search for a ferromagnetic phase in a heavily overdoped nonsuperconducting copper oxide. *Proc. Natl. Acad. Sci.* **107**, 17131–17134 (2010).
- [15] Ding, Y. *et al.* Disappearance of Superconductivity and a Concomitant Lifshitz Transition in Heavily-Overdoped  $\text{Bi}_2\text{Sr}_2\text{CuO}_6$  Superconductor Revealed by Angle-Resolved Photoemission Spectroscopy. *Chinese Phys. Lett.* **36**, 017402 (2019).
- [16] Li, Z. X., Kivelson, S. A. & Lee, D. H. Superconductor-to-metal transition in overdoped cuprates. *npj Quantum Mater.* **6**:36 (2021).
- [17] Piriou, A., Jenkins, N., Berthod, C., Maggio-Aprile, I. & Fischer. First direct observation of the Van Hove singularity in the tunnelling spectra of cuprates. *Nat. Commun.* **2**:221 (2011).
- [18] Li, X. *et al.* Quasiparticle interference and charge order in a heavily overdoped non-superconducting cuprate. *New J. Phys.* **20**, 063401 (2018).
- [19] McElroy, K. *et al.* Relating atomic-scale electronic phenomena to wave-like quasiparticle states in. *Nature* **422**, 592–596 (2003).
- [20] Kohsaka, Y. *et al.* How Cooper pairs vanish approaching the Mott insulator in  $\text{Bi}_2\text{Sr}_2\text{CaCu}_2\text{O}_{8+\delta}$ . *Nature* **454**, 1072–1078 (2008).
- [21] Fujita, K. *et al.* Simultaneous transitions in cuprate momentum-space topology and electronic symmetry breaking. *Science* **344**, 612–616 (2014).
- [22] Kohsaka, Y. *et al.* An intrinsic bond-centered electronic glass with unidirectional domains in underdoped cuprates. *Science* **315**, 1380–1385 (2007).
- [23] Wise, W. D. *et al.* Imaging nanoscale Fermi-surface variations in an inhomogeneous superconductor. *Nat. Phys.* **5**, 213–216 (2009).
- [24] Lawler, M. J. *et al.* Intra-unit-cell electronic nematicity of the high-T<sub>c</sub> copper-oxide pseudogap states. *Nature* **466**, 347–351 (2010).

- [25] Hamidian, M. H. *et al.* Detection of a Cooper-pair density wave in  $\text{Bi}_2\text{Sr}_2\text{CaCu}_2\text{O}_{8+x}$ . *Nature* **532**, 343–347 (2016).
- [26] Hashimoto, M. *et al.* Particle-hole symmetry breaking in the pseudogap state of  $\text{Bi2201}$ . *Nat. Phys.* **6**, 414–418 (2010).
- [27] He, R. H. *et al.* From a single-band metal to a high-temperature superconductor via two thermal phase transitions. *Science* **331**, 1579–1584 (2011).
- [28] Battisti, I., Verdoes, G., Van Oosten, K., Bastiaans, K. M. & Allan, M. P. Definition of design guidelines, construction, and performance of an ultra-stable scanning tunneling microscope for spectroscopic imaging. *Rev. Sci. Instrum.* **89**, 123705 (2018).
- [29] Zeljkovic, I. *et al.* Scanning tunnelling microscopy imaging of symmetry-breaking structural distortion in the bismuth-based cuprate superconductors. *Nat. Mater.* **11**, 585–589 (2012).
- [30] Fujita, K. *et al.* Direct phase-sensitive identification of a d-form factor density wave in underdoped cuprates. *Proc. Natl. Acad. Sci.* **111**, (2014).
- [31] Jain, V. & Seung, H. S. Natural image denoising with convolutional networks. *Adv. Neural Inf. Process. Syst. 21 - Proc. 2008 Conf.* 769–776 (2009).
- [32] Zhang, K., Zuo, W., Chen, Y., Meng, D. & Zhang, L. Beyond a Gaussian denoiser: Residual learning of deep CNN for image denoising. *IEEE Trans. Image Process.* **26**, 3142–3155 (2017).
- [33] Weigert, M. *et al.* Content-aware image restoration: pushing the limits of fluorescence microscopy. *Nat. Methods* **15**, 1090–1097 (2018).
- [34] Lehtinen, J. *et al.* Noise2Noise: Learning image restoration without clean data. *Proc. 35th Int. Conf. Mach. Learn.* PMLR **80**:2965–2974 (2018).
- [35] Hendriksen, A. A., Pelt, D. M. & Batenburg, K. J. Noise2Inverse: Self-supervised deep convolutional denoising for linear inverse problems in imaging. *IEEE Trans. Comp. Imag.* **6**, 1320–1335 (2020).
- [36] Krull, A., Buchholz, T. O. & Jug, F. Noise2void-Learning denoising from single noisy images. *Proc. IEEE/CVF Conf. Comput. Vis. Pattern Recognit.* 2124–2132 (2019).
- [37] Batson, J. & Royer, L. Noise2Self : Blind Denoising by Self-Supervision. *Proc. 36th Int. Conf. Mach. Learn.* PMLR **97**:523–533 (2019).
- [38] Hendriksen, A. A. *et al.* Deep denoising for multi-dimensional synchrotron X-ray tomography without high-quality reference data. *Sci. Rep.* **11**:11895 (2021).
- [39] Presland, M. R., Tallon, J. L., Buckley, R. G., Liu, R. S. & Flower, N. E. General trends in oxygen stoichiometry effects on  $T_c$  in Bi and Tl superconductors. *Physica C* **176**, 95–105 (1991).
- [40] Mao, X.-J., Shen, C. & Yang, Y.-B. Image Restoration Using Very Deep Convolutional Encoder-Decoder Networks with Symmetric Skip Connections. *Adv. Neural Inf. Process. Syst. 29 - Proc. 2016 Conf.* 2802–2810 (2016).

- [41] Ronneberger, O., Fischer, P., Brox & T. U-Net: Convolutional Networks for Biomedical Image Segmentation. In: International Conference on Medical Image Computing and Computer-Assisted Intervention. 234-241 (Springer 2015).
- [42] Hashimoto, M. *et al.* Doping evolution of the electronic structure in the single-layer cuprate  $\text{Bi}_{2-x}\text{Sr}_{2-x}\text{La}_x\text{CuO}_{6+\delta}$ : Comparison with other single-layer cuprates. *Phys. Rev. B*. **77**, 094516 (2008).
- [43] Zhong, Y. *et al.* Differentiated roles of Lifshitz transition on thermodynamics and superconductivity in  $\text{La}_{2-x}\text{Sr}_x\text{CuO}_4$ . *Proc. Natl. Acad. Sci.* **119**:32 (2022).
- [44] Berben, M. *et al.* Superconducting dome and pseudogap endpoint in Bi2201. *Phys. Rev. Mater.* **6**, 044804 (2022).
- [45] Putzke, C. *et al.* Reduced Hall carrier density in the overdoped strange metal regime of cuprate superconductors. *Nat. Phys.* **17**, 826–831 (2021).
- [46] Miao, H. *et al.* Charge density waves in cuprate superconductors beyond the critical doping. *npj Quantum Mater.* **6**:31 (2021).
- [47] Kurashima, K. *et al.* Development of Ferromagnetic Fluctuations in Heavily Overdoped  $(\text{Bi,Pb})_2\text{Sr}_2\text{CuO}_{6+\delta}$  Copper Oxides. *Phys. Rev. Lett.* **121**, 57002 (2018).